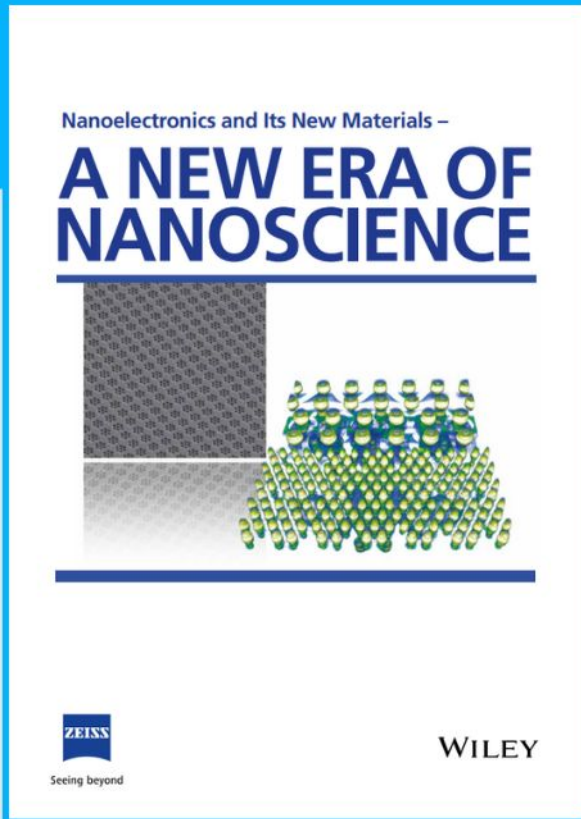# Nanoelectronics and Its New Materials – A NEW ERA OF NANOSCIENCE

Discover the recent advances in electronics research and fundamental nanoscience.

Nanotechnology has become the driving force behind breakthroughs in engineering, materials science, physics, chemistry, and biological sciences. In this compendium, we delve into a wide range of novel applications that highlight recent advances in electronics research and fundamental nanoscience. From surface analysis and defect detection to tailored optical functionality and transparent nanowire electrodes, this eBook covers key topics that will revolutionize the future of electronics.

To get your hands on this valuable resource and unleash the power of nanotechnology, simply download the eBook now. Stay ahead of the curve and embrace the future of electronics with nanoscience as your guide.

MXene-Composite-Enabled Ultra-long-Distance Detection and Highly Sensitive Self-Powered Noncontact Triboelectric Sensors and Their Applications in Intelligent Vehicle Perception

Cong Zhao, Zhaoyang Wang, Yawei Wang, Zian Qian, Zheng Tan, Qingyu Chen, Xinxiang Pan, Minyi Xu,* and Ying-Chih Lai*

With the ongoing advancement in sensor technologies, the development of intelligent, secure, and low-carbon vehicles will be possible in the near future. However, providing continuous power to numerous onboard sensors consumes substantial amounts of power from vehicle, resulting in the shortened running times. Herein, a self-powered noncontact triboelectric nanogenerator (SNC-TENG) with ultralong-distance detection and a high sensitivity is proposed, which can be used as ambient perception sensors for smart vehicles. The SNC-TENG is constructed from a MXene/silicone nanocomposite with a fully embedded conductive sponge, which significantly enriches the tribo-charges and leads to an excellent capability and performance. This SNC-TENG is capable of perceiving human activity from a distance of 2 m. To the best of authors knowledge, the perceiving distance per unit area of this SNC-TENG is the highest among previously reported non-contact TENGs. Furthermore, the applicability of the SNC-TENG is explored for vehicle sentry mode and blind spot detection for the first time. The use of this technology in a real vehicle demonstrates its feasibility for use in practical applications. Overall, this study provides a new design scheme for contactless self-powered sensors, and the presented SNC-TENG is expected to be applicable in various fields where non-contact sensing is required.

1. Introduction

Environmental perception technologies fulfill a vital function in terms of improving the safety and reliability of intelligent vehicles.[1–4] They can provide more intuitive information on the surroundings for the decision-making of autonomous vehicles comparing with the method of monitoring drivers.[5–7] For example, forward-looking sensors, such as radar, visible-light cameras (VLCs), and light detection and ranging (LiDAR), are commonly applied in the detection of surrounding objects.[8,9] Although VLCs record information regarding surrounding vehicles and pedestrians,[10] they are unreliable in low-illumination environments and adverse weather conditions, thereby reducing the detection accuracy.[11,12] In addition, although LiDAR can detect surrounding objects under darkness using the scanning laser,[9] it is susceptible to weather conditions.[13] And, the high cost of this technology limits its widespread

C. Zhao, Z. Wang, Y. Wang, Z. Qian, X. Pan, M. Xu
Dalian Key Lab of Marine Micro/Nano Energy and Self-powered Systems
Marine Engineering College
Dalian Maritime University
Dalian 116026, China
E-mail: xuminyi@dlmu.edu.cn
Z. Tan
Transportation Engineering College
Dalian Maritime University
Dalian 116026, China
Q. Chen
Information Science and Technology College
Dalian Maritime University
Dalian 116026, China

X. Pan
School of Electronics and Information technology
Guangdong Ocean University
Zhanjiang 524088, China
Y.-C. Lai
Department of Materials Science and Engineering
National Chung Hsing University
Taichung 40227, Taiwan
E-mail: yclai@nchu.edu.tw
Y.-C. Lai
Innovation and Development Center of Sustainable Agriculture
i-Center for Advanced Science and Technology
National Chung Hsing University
Taichung 40227, Taiwan

**ADVANCED
SCIENCE NEWS**

www.advancedsciencenews.com

**ADVANCED
FUNCTIONAL
MATERIALS**

www.afm-journal.de

application in the automotive industry.[14] Furthermore, the commonly used radar sensors detect their surroundings through radio waves.[9,15,16] However, the provision of continuous power to these conventional sensors not only increases the vehicle power consumption but also dissatisfies the aspirational goals of low-carbon vehicles.[17–19] More importantly, the requirement of additional power sources or batteries inevitably increases manufacturing costs, safety risks, and environmental pollution.[18–20] It is therefore necessary to develop low-power consumption, low-cost, and adaptive sensors to address these issues.

Triboelectric nanogenerators (TENGs), which are based on a combination of triboelectrification and electrostatic induction, can convert mechanical energy into electricity. TENGs have been employed as self-powered sensors in a range of fields, including robotics perception, wearable electronics, and industry monitoring, owing to their wide material availability, high performances, and cost-effectiveness.[21–28] Importantly, TENGs are able to function in noncontact scenarios.[29–41] Since friction with other objects or with the air imparts most daily objects with a surface electrostatic charge,[39] noncontact TENGs can perceive the charged objects with no requirement for physical contact. As such, the working principle of the noncontact TENGs differs from those of the radar and LiDAR technologies; the sensing performances of noncontact TENGs have therefore received growing research attention in recent years.[29–41] For example, a triboelectric touch-free screen sensor has been proposed for recognizing the gestures of the operators.[32] In addition, a self-healing, anti-impact TENG was designed as a noncontact sensor for safeguarding and 3D morphological awareness.[40] However, the centimeter-level detection capacity and the low charge densities of triboelectric materials largely limit the potential of noncontact TENGs sensors. In previous works, various strategies have been proposed to enhance the surface charge densities of noncontact TENGs, such as surface patterning, ion injection, and material optimization.[30,41–44] For example, an ultrathin noncontact TENG was designed using high-permittivity calcium copper titanate ($CaCu_3Ti_4O_{12}$).[33] And, a spherical multiple physical network-based TENG was developed by controlling the Rayleigh instability deformation of the spinning jet and the vapor-induced phase separation that occurs during electrostatic spinning. As a result, a sensing distance of 70 cm was achieved;[41] however, the complicated preparation process impedes the large-scale applicability of such devices. Despite such efforts, the maximum sensing ranges of most noncontact TENGs remain limited, and the achievement of long-distance detection requires relatively large devices.[38] It is therefore necessary to explore an effective strategy to increase the noncontact sensing performances of TENGs to enable long-range detection.

Thus, we herein present a self-powered noncontact triboelectric nanogenerator (SNC-TENG) based on an MXene/silicone nanocomposite and a fully embedded conductive sponge. The proposed sensor can actively perceive the proximity via the electrostatic induction effect. Two optimization strategies are proposed for enhancing the noncontact sensing performance of the SNC-TENG. First, the incorporated MXene ($Ti_3C_2T_x$) nanosheets raise the tribo-charge density by improving the charge trapping capacity. Second, the fully embedded conductive sponge with a network structure enlarges the electrode area in the electrostatic field to increase the number of induced charged carries in the electrode. By optimizing the materials and structure, the device exhibits ultra-long-distance detection (2 m) and high sensitivity (detecting 1 mm movement). To the best of our knowledge, the perceiving distance per unit area of the TENG is the highest among the reported noncontact TENGs. The outputs of the SNC-TENG dependent on the distance, frequency, moving increment, and area are systematically investigated. Moreover, application of the developed SNC-TENG is demonstrated in various smart car applications, including the sentry mode and blind spot detection. Finally, the SNC-TENG is attached to real vehicles to detect approaching persons and to highlight its potential for use in practical applications.
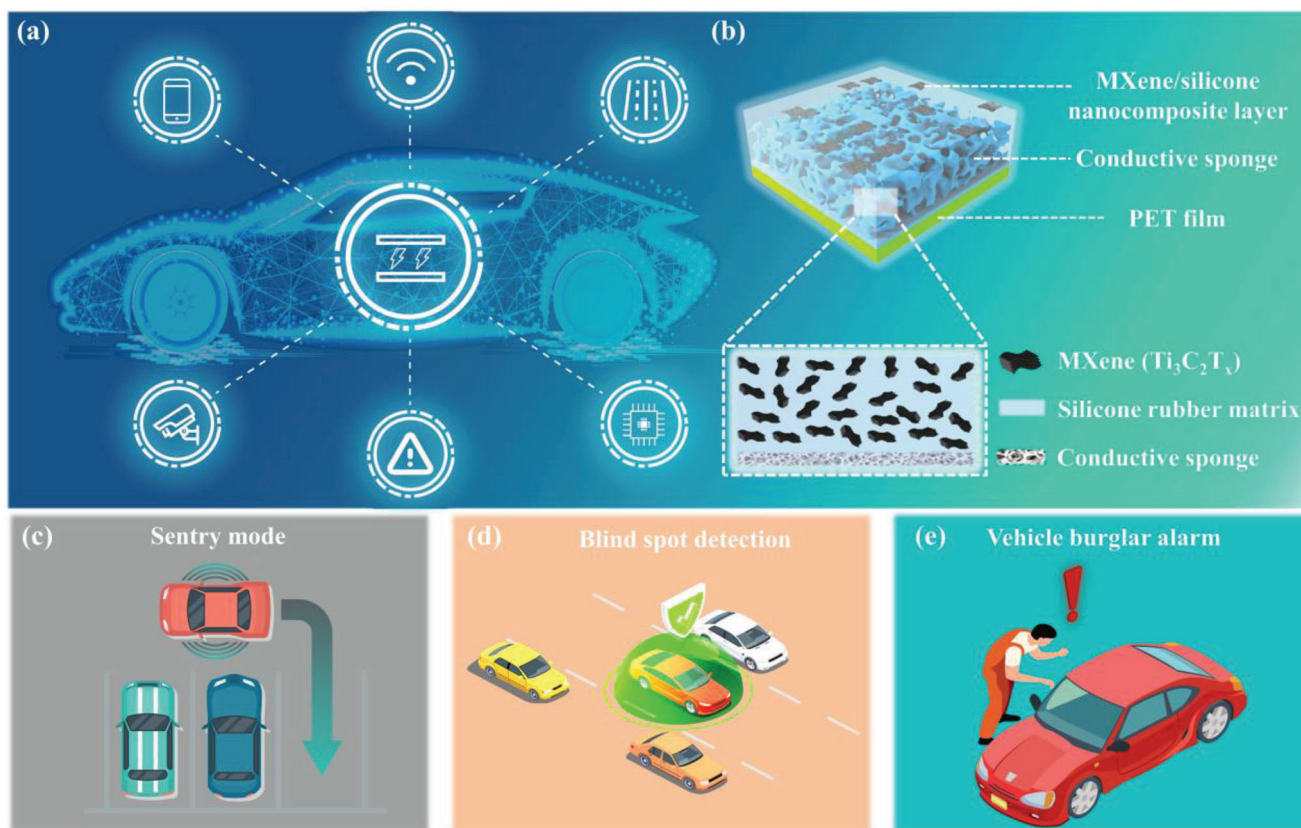
2. Results and Discussion

2.1. Device Structure

Figure 1a illustrates the application scenario of the designed SNC-TENG, which serves to communicate information from the surrounding environment to the intelligent vehicle. A schematic representation of the SNC-TENG structure is given in Figure 1b, wherein it can be seen that the device comprises a fully embedded conductive sponge as the electrode, and an MXene/silicone nanocomposite as the triboelectric layer. The tight bonding between the triboelectric layer and the electrode enables the SNC-TENG to possess structural reliability, which can prevent physical detachment of the two components during long-term operation. In addition, a polyethylene terephthalate (PET) film substrate is adhered to the back of the conductive sponge, silicone rubber is used as the dielectric material due to its high electron affinity and flexibility,[26,27,45,46] and MXene ($Ti_3C_2T_x$) nanosheets are employed due to their high electronegativity and excellent capability in trapping charges.[41,42,44,47,48] Thus, the MXene nanosheets were mixed with the silicone rubber matrix to further improve the noncontact perceiving performance of the SNC-TENG. It was considered that the designed SNC-TENG, as a self-powered noncontact sensor, exhibits potential for use in a range of functions, including in the vehicle sentry mode, in blind spot detection, and in burglar alarms, as depicted in Figure 1c–e.

2.2. Fabrication and Characterization of the SNC-TENG

Figure 2a gives a schematic illustration of the fabrication process used to prepare the SNC-TENG. This process avoids the use of complex equipment and strict preparation temperatures, thereby indicating its superiority in terms of large-scale manufacturing. Figure 2b shows the field emission scanning electron microscopy (FESEM) images of the MXene nanosheets, in which a multilayer structure can be seen. In addition, the X-ray photoelectron spectroscopy (XPS) survey spectrum (Figure 2c) indicates the presence of Ti, F, O, and C in MXene nanosheets.[44] An FESEM image of the conductive sponge is shown in Figure 2d, wherein the network structure can be observed. The results of energy dispersive spectrometry (EDS) mapping are presented in Figure S1 (Supporting Information), and reveal the presence of Ni, Cu, Si, C, and O at the surface of the conductive sponge. Furthermore, as shown in Figure 2e and Figure S1f (Supporting Information),

**ADVANCED
SCIENCE NEWS**
www.advancedsciencenews.com

**ADVANCED
FUNCTIONAL
MATERIALS**
www.afm-journal.de

Figure 1. Schematic representation of the structure and application scenarios of the developed SNC-TENG. a) Prospects of applying the SNC-TENG in an intelligent vehicle. b) Configuration of the SNC-TENG. c–e) Potential applications in sentry mode, blind spot detection, and burglar alarms.
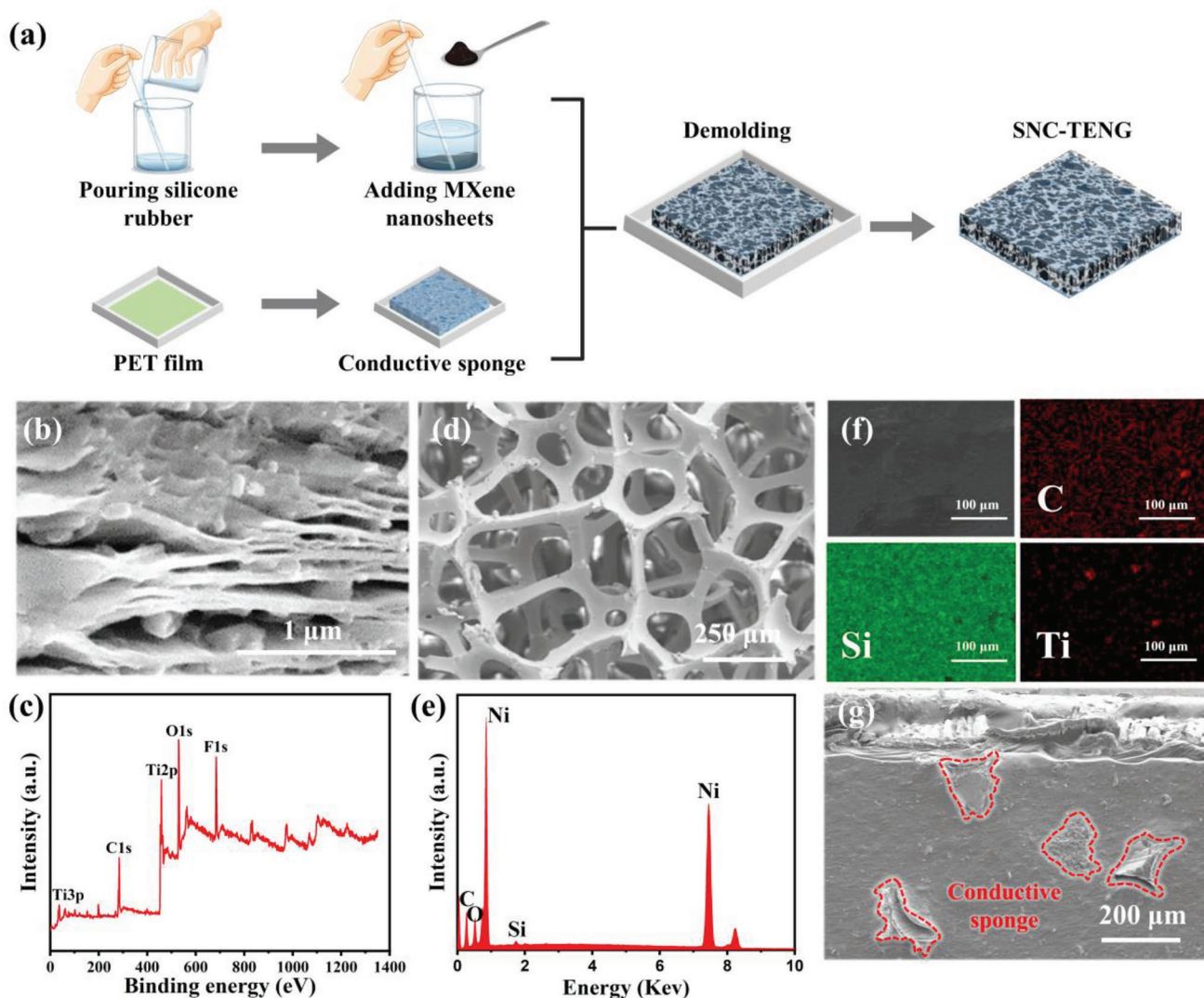
the atomic percentage of Ni is 84.3%, thereby indicating that the conductive sponge possesses electrical conductivity at the surface of its network structure. A top-view FESEM and the EDS elemental analysis (Figure 2f; Figure S2, Supporting Information) of the MXene/silicone layer indicate a wide distribution of C, Si, and Ti, wherein the Si and Ti are derived from the silicone rubber and the MXene nanosheets, respectively. These results reveal that the MXene nanosheets are uniformly encapsulated throughout the silicone rubber. A cross-sectional FESEM image of the SNC-TENG is shown in Figure 2g, in which it is apparent that the MXene/silicone nanocomposite penetrates into the network of the conductive sponge.

2.3. Optimization of the SNC-TENG

The charge density is crucial in determining the sensing ability of the noncontact TENG.[41] Thus, for optimization purposes, three types of contact–separation (CS) mode TENGs are prepared with additional nylon and Al films, as shown in **Figure 3**a.[49] The sample thickness was set as 1.5 mm in all cases, and the working principle of the CS-mode TENG was based on tribo-electrification and electrostatic induction (Figure S3, Supporting Information).[49] As shown in Figure 3b and Figure S4 (Supporting Information), compared to the pure silicone rubber-based device, the open-circuit voltage (V_{oc}), short-circuit charge (Q_{sc}),

and short-circuit current (I_{sc}) were larger for the TENG wherein the MXene/silicone nanocomposite was coated on the conductive fabric. This high electrical output can be attributed to the large tribo-charge trapping capacity of the MXene nanosheets, as depicted in Figure 3a(ii).[44,50] At the beginning of the contact electrification process, positive and negative tribo-charges are generated on the surface of the nylon film and on the dielectric layer of the TENG, respectively. When the nylon and the dielectric layer are separated, the negative tribo-charges on the dielectric layer can induce positively charged carriers in the conductive fabric. The established electric field between the surface of the dielectric layer and the conductive fabric can make the surface negative tribo-charges drift toward the conductive fabric. At this stage, the MXene nanosheets can effectively trap the drifting tribo-charges. Thus, continuously contact and separation are capable of bringing more tribo-charges in the dielectric layer, thereby resulting in an enhanced electrical output.

Moreover, the V_{oc}, Q_{sc}, and I_{sc} values of the TENG containing the fully embedded conductive sponge reached 251.8 V, 65.3 nC, and 2.2 µA, which are significantly higher than those of the CS-mode TENG based on the conductive fabric (Figure 3b; Figure S4, Supporting Information). This enhancement can be explained by considering that full embedding of the conductive sponge in the dielectric layer increases the effective area of the electrode in the electrostatic field. The effect of electrostatic induction is therefore enhanced, which in turn leads to an increase in the amount
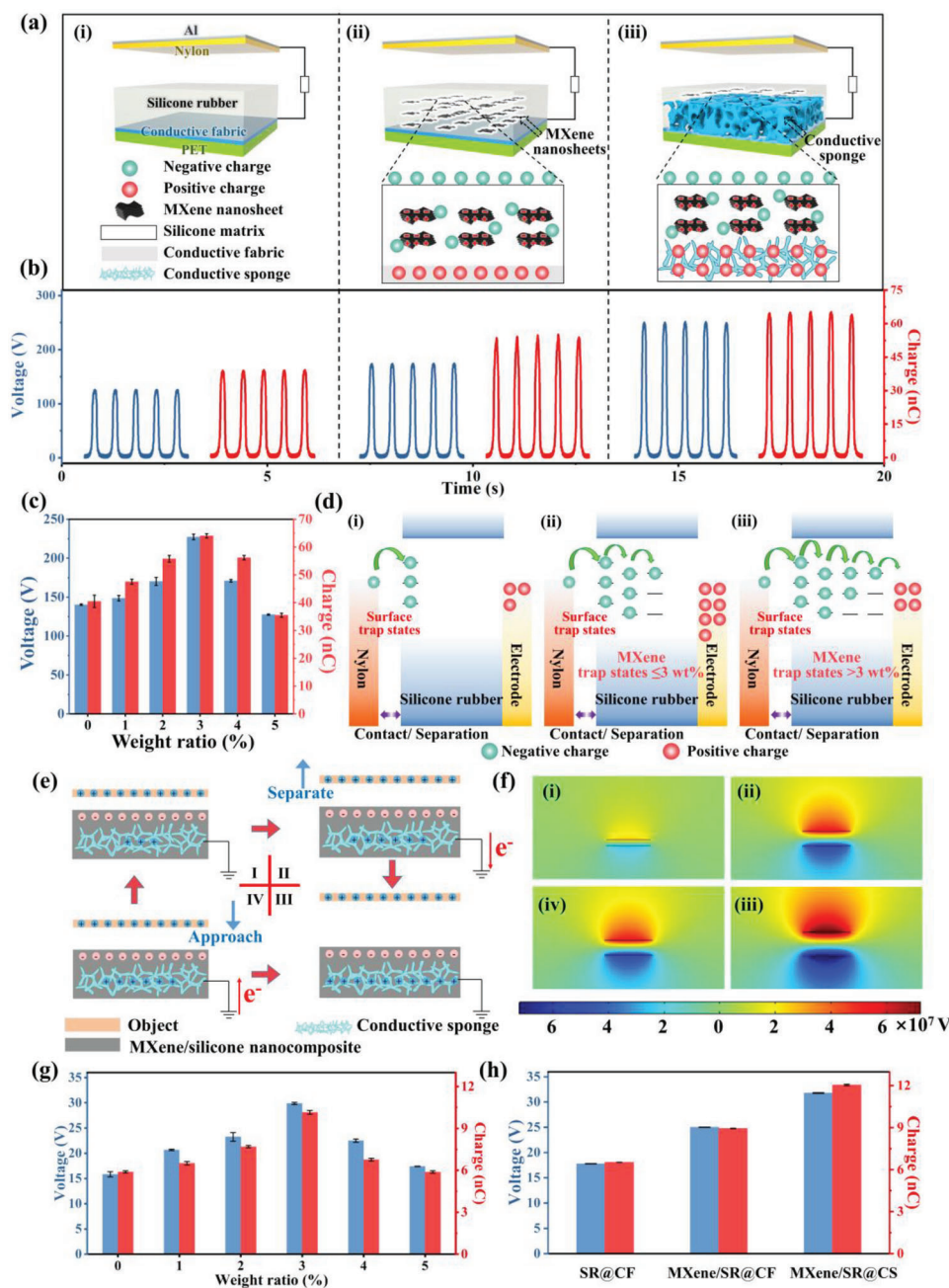
Figure 2. Fabrication and material characterization of the SNC-TENG. a) Schematic diagram outlining the SNC-TENG fabrication process. b) FESEM image of the MXene nanosheets. c) XPS survey spectrum of the MXene nanosheets. d) FESEM image of the conductive sponge. e) Element analysis of conductive sponge. f) EDS mapping analysis of the MXene/silicone nanocomposite layer. g) Cross-sectional FESEM image of the SNC-TENG.

of induced charges (Figure 3a(iii)). Improvement of the noncontact TENG performance can therefore be achieved through material optimization (i.e., mixing the MXene nanosheets with the silicone matrix), and structural optimization (i.e., by fully embedding the conductive sponge).

The effect of the MXene nanosheets weight ratio on the electrical performance of the CS-mode TENG was investigated quantitatively by applying the same contact force of 20 N and frequency of 2 Hz. As shown in Figure 3c and Figure S5 (Supporting Information), the values of V_{oc}, Q_{sc}, and I_{sc} increased as the MXene nanosheet weight ratio was increased from 0 to 3 wt%, indicating its obvious effect in enhancing the electrical performance of the TENG. However, a further increase in the weight ratio led to a poorer electrical performance. The mechanism of above results can be more specifically described in Figure 3d. After the contact and separation of the nylon and silicone rubber, the negative tribo-charges (green dots) on the dielectric layer are stored

in the trap states of the silicone rubber and induce the accumulation of positive carriers (red dots) in the conductive sponge, leading to the formation of an electric field.[51,52] When pure silicone rubber was used as the dielectric layer, only the negative tribo-charges trapped at the surface of the silicone rubber can create an electrostatic field to induce positive charges in the conductive sponge (Figure 3d(i)). As the MXene nanosheets doped in the silicone rubber, the negative tribo-charges can penetrate and be trapped in the MXene nanosheets of silicone rubber matrix (Figure 3d(ii)). As a result, large amount of negative tribo-charges in the dielectric layer can form an enhanced electrostatic field, leading to an increased output. However, upon increasing the weight ratio of the MXene nanosheets >3 wt%, conductive paths can be formed by the nanocomposite, thereby promoting negative tribo-charges to drift into the conductive sponge, and declining the electrical performance of the TENG (Figure 3d(iii)). We further investigated the performance of the device in responding

Figure 3. Optimization of the electrical performance. a) Schematic illustration of the three types of CS-mode TENGs and their corresponding working mechanisms. b) Generated V_{oc} and Q_{sc} for the CS-mode TENGs depending on the type of structures. c) Variation in the V_{oc} and Q_{sc} values of the CS-mode TENGs at various MXene nanosheet weight ratios. d) Energy level illustration and the corresponding charge transfer and trapping process. e) Schematic representation of the SNC-TENG working principle under noncontact mode. f) Electrical potential distributions of the SNC-TENG simulated using COMSOL software. g) Generated V_{oc} and Q_{sc} for the SNC-TENG depending on the MXene nanosheet weight ratio under noncontact mode conditions. h) Generated V_{oc} and Q_{sc} for the SNC-TENGs depending on the types of structure under noncontact mode conditions.

to various contact forces. As shown in Figure S6a–c (Supporting Information), the V_{oc}, Q_{sc}, and I_{sc} increase as the applied force varies from 1 to 20 N. Subsequently, the growth rates of the outputs decelerate as the forces increase. The results reveal that the MXene/silicone-based TENG can function as a pressure sensor for detecting the contact forces. Comparing with the previously MXene-based devices,[53–56] the feature of actively self-powered

response can minimize the power consumption of the sensing device.

On the basis of the above electrostatic induction, this SNC-TENG is able to work in the noncontact single-electrode mode, as illustrated in Figure 3e. More specifically, it can be seen that the MXene/silicone nanocomposite layer of the SNC-TENG is negatively charged, and some positive charges are accumulated in the

electrode of the SNC-TENG to balance the electrostatic charges (step I). As the positively charged object moves away from the SNC-TENG, the electrons begin to flow from the electrode to the ground through the external circuit (step II). Subsequently, as the object continues to move away from the SNC-TENG, and the number of charges transferred from the electrode to the ground will achieve the maximum value (step III). Conversely, as the object gradually approaches, the electrode will attract the electrons from the ground to achieve electrical equilibrium (step IV). Likewise, if the object is negatively charged, the process of electron transferred between the conductive sponge and the ground will be reversed. To verify the working mechanism, the corresponding potential distribution was simulated using COMSOL software, as presented in Figure 3f. It was found that the potential difference between the SNC-TENG and the charged object changes correspondingly during the process of approach and separation.

The effect of the MXene nanosheet weight ratio on the perceiving performance of the SNC-TENG was subsequently evaluated in the noncontact single-electrode mode. Figure 3g and Figure S7 (Supporting Information) display the V_{oc}, Q_{sc}, and I_{sc} values obtained for the SNC-TENG as the MXene nanosheet weight ratio was increased from 0 to 5 wt%. As indicated, upon increasing the MXene weight ratio from 0 to 3 wt%, the V_{oc}, Q_{sc}, and I_{sc} values were improved from 15.8 V, 5.9 nC, and 88.2 nA to 29.9 V, 10.1 nC, and 165.7 nA, which represent increases of 1.9, 1.7, and 1.9 times compared to the values obtained for the SNC-TENG based on pure silicone rubber. However, the electrical output of the SNC-TENG decreased as the MXene weight ratio was increased further to 5 wt%. These trends are consistent with those presented in Figure 3c and Figure S5 (Supporting Information), indicating that the addition of MXene nanosheets can improve the noncontact sensing performance at an optimal weight ratio of 3 wt%. Figure 3h and Figure S8 (Supporting Information) also demonstrate that the SNC-TENG based on the fully embedded conductive sponge performs better than that based on conductive fabrics under noncontact mode conditions, thereby revealing the effectiveness of this structural design strategy in terms of improving the noncontact sensing performance.
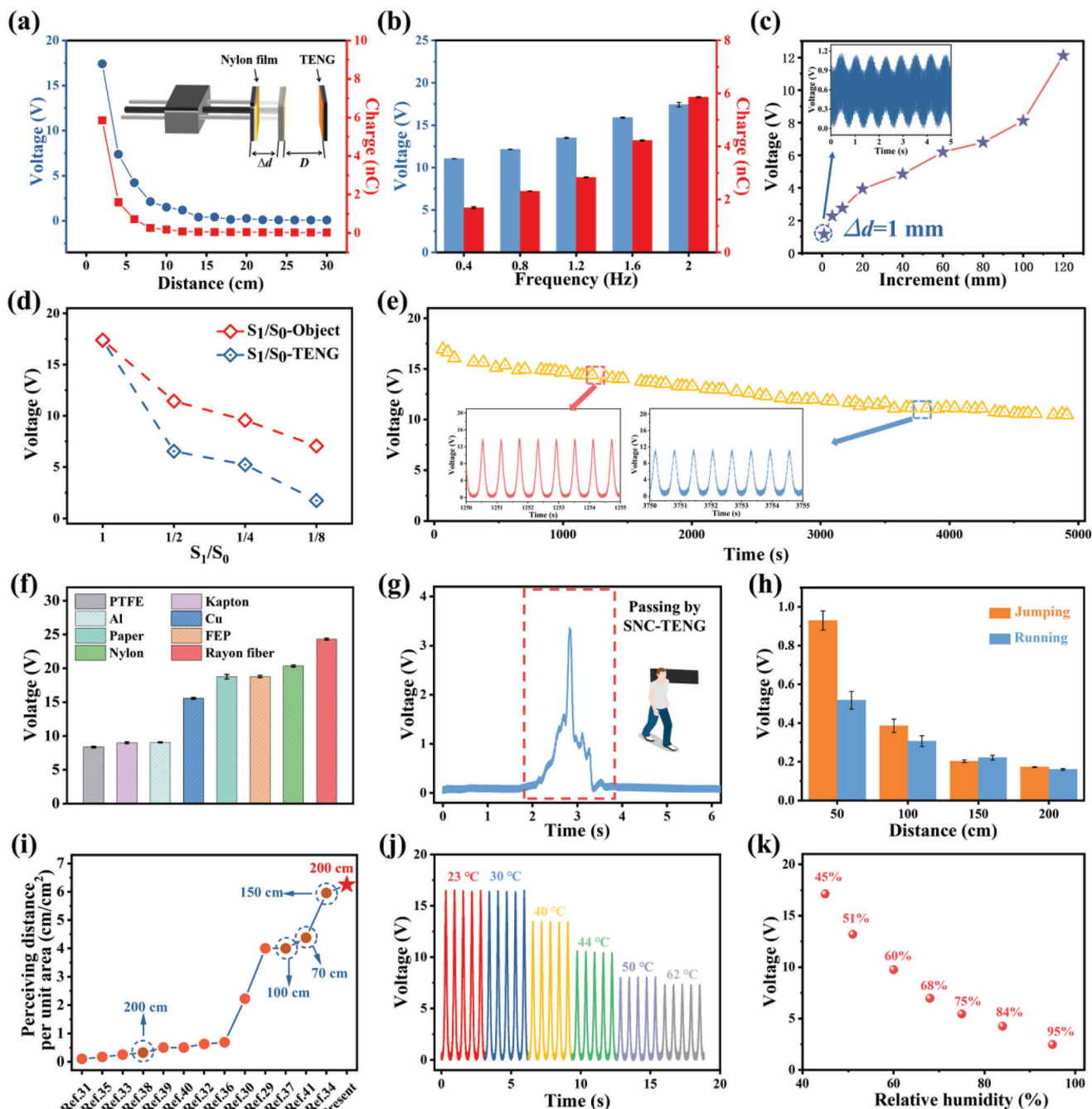
2.4. Noncontact Sensing Performance of the SNC-TENG

Subsequently, the electrical output of the SNC-TENG was investigated in detail under vertical noncontact mode conditions. As shown in the inset of **Figure 4**a, a positively charged-nylon film (the triboelectrified layer) is attached to one end of a linear motor to simulate a moving object. The negatively charged SNC-TENG (dimensions: 8×4 cm^2) is placed at a distance of d from the approaching end of the positively charged nylon film. The moving increment (Δd) and frequency (f) of the nylon film can be precisely adjusted using the linear motor. As shown in Figure 4a and Figure S9 (Supporting Information), the V_{oc}, Q_{sc}, and I_{sc} values of the SNC-TENG decrease as the distance is increased from 2 to 30 cm, and this can be attributed to attenuation of the electrostatic field with a longer distance. As shown in Figure 4b, both the V_{oc} and Q_{sc} values of the SNC-TENG increase as the moving frequency of the nylon film was increased from 0.4 to 2 Hz at a fixed d of 2 cm (the generated I_{sc} is shown in Figure S10 (Supporting Information)). This can be accounted for by considering

that the increasing moving frequency enables a greater degree of charge transfer between the nylon film and the air, resulting in an increased number of carried charges in the nylon film.[57] Additionally, the V_{oc}, Q_{sc}, and I_{sc} values of the SNC-TENG were found to increase as the Δd of the nylon film was increased from 1 to 140 mm, as shown in Figure 4c and Figure S11 (Supporting Information). It should be noted here that the SNC-TENG exhibits a high sensitivity even for a slight movement increment of 1 mm (see the voltage signal presented in the inset of Figure 4c).

To test the effects of the electrified object and SNC-TENG areas on the noncontact sensing performance, the S_1/S_0 ratio was used to define the variation in size, where S_1 is the area after cutting and S_0 is the original area. As shown in Figure 4d and Figure S12 (Supporting Information), the V_{oc}, Q_{sc}, and I_{sc} values of the SNC-TENG decreased with a reduction in the nylon film and device areas, thereby demonstrating that the SNC-TENG is more sensitive to larger objects, and that expanding the area of the noncontact TENG can enhance the noncontact sensing capacity. As mentioned above, this device can be easily fabricated on a large scale, and so it should be possible to enhance its noncontact sensing ability for additional applications by enlarging the device area. The response time is investigated for evaluating the performance of the device in acquiring the real-time signal. As shown in Figure S13 (Supporting Information), the displacement waveforms of the objectives exhibit excellent synchronization with the corresponding electrical signal of the device. And, the response time of the device is less than 30 ms.

The durability of the SNC-TENG was then examined through a number of continuous approach/separation cycles using the nylon film. As indicated in Figure 4e, although the generated V_{oc} tends to slowly decline, the SNC-TENG is still able to deliver an appropriate electric signal for a considerable period of 5000 s. In addition, the shape of the electrical signal remains relatively constant, as depicted in the inset of Figure 4e. In addition, the response of the SNC-TENG to various materials (e.g., PTFE, Kapton, Al, Cu, paper, FEP, nylon, and rayon fiber) was then evaluated at a fixed f of 1.6 Hz and d of 2 cm. As shown in Figure 4f, the value of V_{oc} is related to the electropositivity of the material being examined. More specifically, the V_{oc} reached 24.3 V when sensing rayon fiber, a common material used for manufacturing clothes. Furthermore, the electrical output of the SNC-TENG from detecting the human skin is investigated in Figure S14 (Supporting Information). The V_{oc} of the device rises from 4.4 to 14.9 V with the increasing of the movement speed of the hand. And, the generated Q_{sc} and I_{sc} can reach 1.9 nC and 120.6 nA, respectively. Figure 4g shows the real-time signal recorded for the SNC-TENG as the volunteer walks past the device at a distance of 30 cm, wherein it can be seen that a peak signal of 3.4 V was reached as Volunteer 1 walks past the device. Figure S15 (Supporting Information) presents comparable results for other volunteers, wherein it is apparent that peak variance was observed due to the different clothing materials worn by volunteers. For example, Volunteer 1 mainly wore rayon fiber, which is an excellent polymer material for sensing by the SNC-TENG, as discussed above (see Figure 4f).

Moreover, the recorded V_{oc} values generated by different types of movement at various distances were recorded (Figure 4h) and it was found that the value of V_{oc} generated by both jumping and running decreases as the distance increases

ADVANCED
SCIENCE NEWS

www.advancedsciencenews.com

ADVANCED
FUNCTIONAL
MATERIALS

www.afm-journal.de

Figure 4. Sensing performance of the SNC-TENG in the vertical noncontact mode. a) Effect of the distance on the V_{oc} and Q_{sc} values. b) Effect of the frequency on the V_{oc} and Q_{sc} values. c) Influence of the moving increment on the V_{oc} value. d) Variation in V_{oc} upon altering the sizes of the electrified layer and the SNC-TENG. e) Durability test for the SNC-TENG. f) Variation in V_{oc} upon response of the SNC-TENG to various materials. g) Output signals recorded when walking past the SNC-TENG. h) V_{oc} values of the SNC-TENG recorded for different activities and distances. i) Comparison of the perceiving distance per unit area of the TENGs prepared in this work with similar previously reported results. Variation in the V_{oc} values of SNC-TENG with the ambient j) relative humidity and k) temperature.

between the device and the volunteer. Notably, the voltage signals generated by jumping are significantly larger than those of running at the same distance, likely due to the motion speed and amplitude of jumping being larger than those of running. Significantly, even at a distance of 200 cm, the volunteer activities

can still be perceived, thereby indicating the outstanding non-contact sensing performance of the SNC-TENG (see Figures S16 and S17, Supporting Information). To the best of our knowledge, this perceiving distance of 200 cm is a record among previously reported noncontact TENGs,[38] and notably, this was achieved

**ADVANCED
SCIENCE NEWS**

www.advancedsciencenews.com

**ADVANCED
FUNCTIONAL
MATERIALS**

www.afm-journal.de

using a TENG with an area of only 8×4 cm^2 (cf, the previously reported A4 paper size). For the purpose of this study, the ratio of d/S was used to evaluate the noncontact sensing capabilities of the TENGs, wherein d and S are the maximum perceived distance and area of the TENG, respectively. As presented in Figure 4i and Table S1 (Supporting Information), the d/S ratio of the SNC-TENG can reach 6.25, which is the highest among previously reported noncontact TENGs, further indicating its outstanding noncontact sensing performance.[29–41] The influences of the ambient temperature and relative humidity on the output of the SNC-TENG were also investigated. As shown in Figures S18 and S19 (Supporting Information), customized experimental setups were constructed, wherein a blower heater and a humidifier were used to control the ambient temperature and the relative humidity, respectively. As shown in Figure 4j, the V_{oc} of the SNC-TENG remains almost constant at temperatures of 23 and 30 °C, although a further increase to 62 °C led to a reduction in V_{oc} (i.e., from 16.5 to 7.3 V) due to the escape of trapped charges from the shallow traps due to higher temperature.[58] Similarly, the generated V_{oc} decreased rapidly as the relative humidity was increased from 45% to 95% (Figure 4k). In this case, the observed reduction was attributed to dissipation of the surface charges due to the formation of a water layer.[50] However, the value of V_{oc} continued to reach 2.5 V even at 95% relative humidity, thereby demonstrating the high adaptability of the SNC-TENG to harsh environments.

Subsequently, the electrical performance of the SNC-TENG was tested under the horizon noncontact mode, as depicted in Figure S20a (Supporting Information). Upon increasing the distance from 2 to 30 cm, the V_{oc}, Q_{sc}, and I_{sc} values decreased from 4.8 V, 1.4 nC, and 59.6 nA to 0.8 V, 0.2 nC, and 42.3 nA, respectively (see Figure S20b–d) (Supporting Information). The values of V_{oc}, Q_{sc}, and I_{sc} were also found to increase with the moving frequency of the object, as shown in Figure S20e–g (Supporting Information). The electrical output of the device decays as the $\triangle d$ of the objective decreases (Figure S20h–j, Supporting Information). The perceiving sensitivity of 1 mm can be remained under the horizon noncontact mode, as shown in the inset of Figure S20h (Supporting Information). These results therefore indicate that the self-powered noncontact SNC-TENG sensor is able to perceive approaching objects from multiple directions.
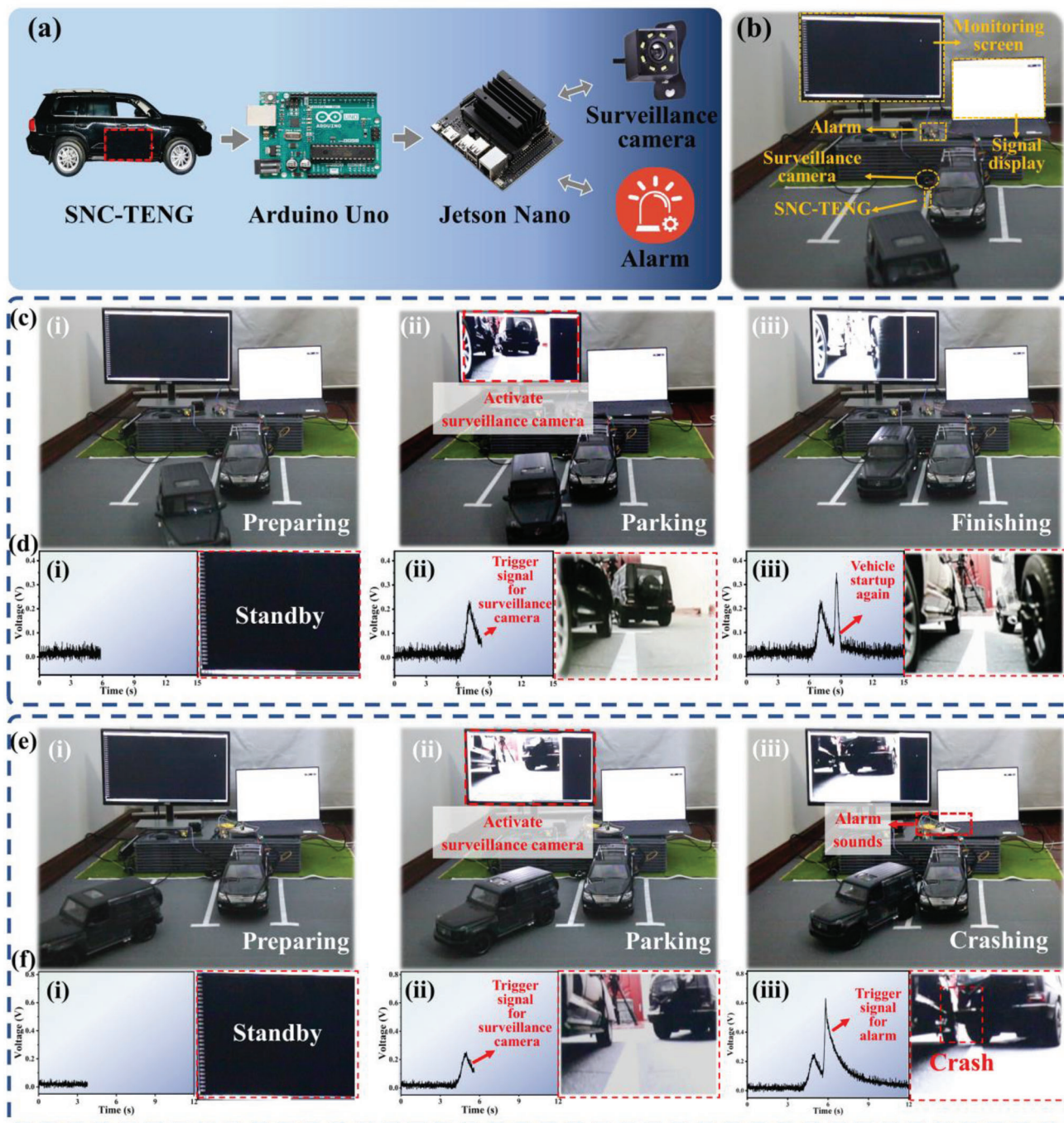
2.5. Demonstration of Potential SNC-TENG Applications

Intelligent vehicles with sentry mode have been developed for assisting parking and preventing theft using conventional passive sensors.[59,60] But, the work of sentry mode relies on continuous operation of the conventional passive sensors, resulting in continuous power consumption. Herein, the use of the designed SNC-TENG as a self-powered noncontact sensor is successfully demonstrated in the vehicle sentry mode. As shown in **Figure 5**a, the SNC-TENG is attached in the surface of the vehicle to perceive the surroundings through the effect of electrostatic induction. The induced signals are acquired by a signal acquisition module (Arduino Uno), and a control program is sent to the surveillance camera through a microprocessor unit (Jet-

son Nano). The surveillance camera is then triggered to switch on and record the surroundings. When the generated signal exceeds the set threshold value, the buzzer can be activated to sound an alarm. For example, Figure 5b and Movie S1 (Supporting Information) show the application of this SNC-TENG as a noncontact sensor for detecting an approaching vehicle in a simulated parking lot. The parking process of the nearby vehicle can be divided into three steps, including preparing, parking, and finishing. Initially, the reversing vehicle is far from the SNC-TENG and the camera remains in the off state (Figure 5c(i)). As the reversing vehicle begins to approach the SNC-TENG (Figure 5c(ii)), an electrical signal of 0.2 V is generated, and the trigger signal activates the surveillance camera to record the approaching vehicle (Figure 5d(ii)). As shown in Figure 5d(ii), the surveillance monitoring screen clearly displays essential information relating to the nearby vehicle (e.g., make, model, and color). When the vehicle finishes the parking process (Figure 5c(iii)) a larger signal of 0.3 V is generated as the vehicle further approaches the SNC-TENG, as indicated in Figure 5d(iii). Since parking accidents often occur owing to driver error, such an accident is simulated in Figure 5e and Movie S1 (Supporting Information). In this case, the SNC-TENG generates an electrical signal of 0.2 V as the reversing vehicle approaches, and the surveillance camera is activated, as shown in Figure 5f(ii). Subsequently, as the reversing vehicle comes into contact with the SNC-TENG, a larger electrical signal of 0.6 V is generated, which exceeds the threshold value of buzzer activation (Figure 5f(iii)) and the alarm sounds (Figure 5e(iii)). The device with the characteristic of shock-absorbing is beneficial for practical applications.[61] Herein, the attached flexible device may also mitigate shocks, thereby reducing the damage to the vehicles caused by the unexpected accidents. And, the crashing accident can be recorded clearly by the surveillance camera (Figure 5f(iii)), which is essential for later accountability, especially in the case of unmonitored parking lots.

Furthermore, the SNC-TENG can be used in the detection of vehicles in the blind spots while driving, as shown in **Figure 6**a and Movie S2 (Supporting Information).[16,62] Figure 6b depicts the process flow from perceiving the approaching vehicles to controlling the virtual vehicles. Two SNC-TENGs, attached on the surface of the vehicle, are utilized to perceive the vehicles approaching from left and right lanes. The data processing unit then acquires the electrical signals from the left-side SNC-TENG (L-TENG) and the right-side SNC-TENG (R-TENG), and delivers a real-time motion command to the virtual vehicles. In this demonstration, the 3D virtual interface is capable of assisting the drivers to observe vehicles approaching from the left or right blind spot. As shown in Figure 6c, the vehicle equipped with the two SNC-TENG devices is in the middle lane of a three-lane road. The electrical signals generated in response to the approaching vehicles enable the corresponding virtual vehicles to move, as shown in Figure 6c(i,ii). Furthermore, simultaneous operation of the L-TENG and R-TENG allows both virtual vehicles to take the action, as can be seen in Figure 6c(iii). It should be noted here that the signals from the R-TENG and the L-TENG are generated in sequence, and this sequence corresponds to the approaching order of the two vehicles in reality, thereby revealing the high sensitivity of these devices.
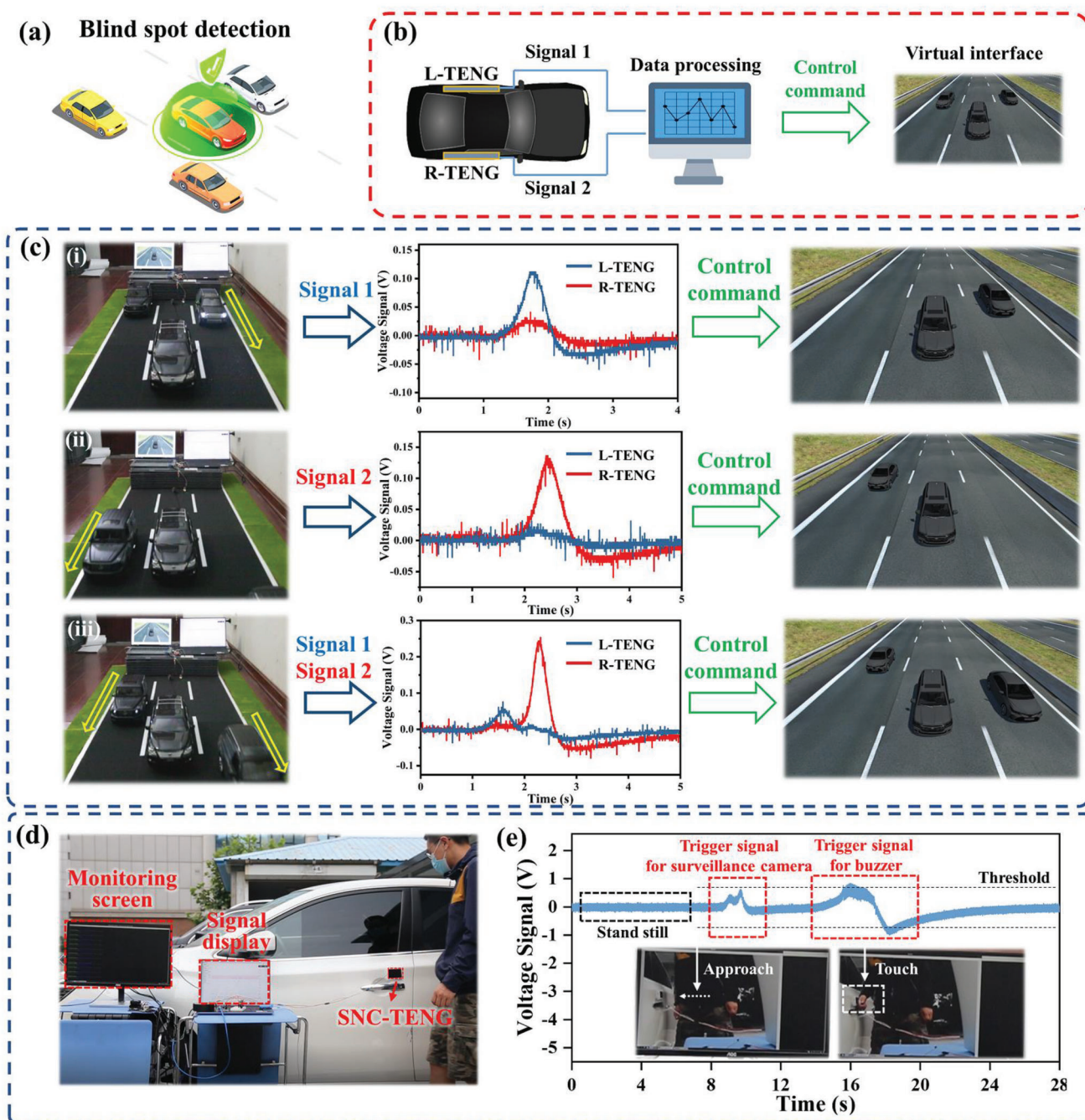
Finally, the SNC-TENG was attached on the surface of a vehicle to determine its potential in detecting a potential break-in

Figure 5. Demonstration of using the SNC-TENG as a noncontact sensor in vehicle sentry mode during parking. a) Logical block diagram of SNC-TENG application in vehicle sentry mode. b) Photographic images of the sentry mode system in a simulated parking lot. c) Photographic images of the three stages involved in detecting surrounding vehicles during parking. d) Real-time signals of SNC-TENG corresponding to the three steps of successful parking, right inset shows the corresponding monitor screen of surveillance camera. e) Photographic images of the three stages involved in a collision during parking. f) Real-time signals of the SNC-TENG corresponding to the three steps of failed parking, right inset shows the corresponding monitor screen of surveillance camera.

(Figure 6d; Movie S3 (Supporting Information)). As depicted in Figure 6e, as the volunteer approaches the vehicle, an electrical signal of 0.6 V is generated by the SNC-TENG. As a result, the surveillance camera on the rearview mirror is activated, and video recording begins, as shown in the inset of Figure 6e. As the volunteer touches the SNC-TENG, a larger electrical signal of 0.8 V is generated, and the buzzer alarm is activated. The demonstration therefore reveals that the SNC-TENG exhibits potential for practical application in detecting varying conditions regarding the surroundings of a vehicle.

**ADVANCED
SCIENCE NEWS**
www.advancedsciencenews.com

**ADVANCED
FUNCTIONAL
MATERIALS**
www.afm-journal.de

Figure 6. Application of the SNC-TENG in blind spot detection and potential theft detection in a real vehicle. a) Representation of the detection of vehicles in the blind spot. b) Process flow from perceiving an approaching vehicle to control of the virtual vehicle. c) Vehicles approaching from i) the left lane, ii) the right lane, and iii) both lanes, and the corresponding actions in virtual interface. d) Photographic image of the SNC-TENG applied to a real vehicle for the detection of potential theft. e) Real-time signal generated by the SNC-TENG for activation of the vehicle alarm. The insets show photographic images of the demonstration process.

3. Conclusion

In summary, a self-powered noncontact TENG with ultra-long detection and high sensitivity was developed to perceive movement and contact via the electrostatic induction effect. This SNC-TENG was optimized by incorporating MXene ($T_3C_2T_x$) nanosheets along with a fully embedded conductive sponge, which led to an enhanced charge density and exceptional performance. The noncontact sensing performance of the SNC-TENG was comprehensively studied under various distances, frequencies, and moving increments. As a result, the device was able to detect human activity (e.g., running and jumping) from a distance of 2 m, and a high

sensitivity of 1 mm movement was demonstrated. These results represent a new record in the perceiving distance per unit area among previously reported noncontact TENGs. The applicability of using this device in sentry mode and blind spot detection purposes was also successfully demonstrated, and the noncontact TENG was applied in a real vehicle to evaluate its performance in detecting potential collisions and theft. The proposed noncontact TENG is particularly desirable due to its self-powered nature, its lower cost compared with conventional onboard sensors, and its suitability for scale-up manufacture. These properties will be expected to accelerate the development of smart and secure vehicles. This work will also be expected to promote advances in a wide range of noncontact sensing technologies.

4. Experimental Section

Materials: Silicone rubber (Dragon SkinTM 30) was purchased from Smooth-On (United States), while the MXene ($Ti_3C_2T_x$) nanosheets were purchased from Foshan Xinxi Technology Co., Ltd. The conductive sponge bearing an adhesive was purchased from Kunshan Electronic Materials Products Co., Ltd.

Fabrication of the SNC-TENG: Initially, the MXene nanosheets were fully ground using a mortar and pestle. Subsequently, parts A and B of Dragon Skin 30 were mixed in equal weights, and the ground MXene nanosheets were added to the liquid silicone rubber and mixed uniformly. A 3D printer was then used to prepare a rectangular acrylic mold (internal dimensions: 8 cm × 4 cm). A PET film (with the thickness of 200 μm) was attached to the bottom of the rectangular mold as an insulating layer. The conductive sponge (dimensions: 7.8 cm × 3.8 cm × 0.05 cm) was pasted onto the surface of the PET film using its adhesive side, and the liquid mixture prepared above was slowly poured onto the top of the conductive sponge slowly. Finally, the mixture was dried at room temperature for 10 h and the dried SNC-TENG was removed from the acrylic mold.

Electrical Measurements: The surface morphologies of the MXene/silicone nanocomposite layer, the MXene nanosheets, and the conductive sponge were characterized by FESEM (Hitachi S-4800). The XPS survey spectrum of the MXene ($Ti_3C_2T_x$) nanosheets was recorded using a Bruker D8 Advance instrument. In addition, the elemental distribution maps of the SNC-TENG were obtained by EDS (Oxford X-MaxN). To measure the electrical performance of the SNC-TENG under the CS mode, an integrated linear motor equipped with a pressure feedback control system (R-LP3) was employed. Furthermore, a linear motor (Linmot E1100) allowing control of the moving increment and frequency was used to evaluate the noncontact sensing performance. It should be noted that the MXene/silicone layer of the SNC-TENG was negatively charged by rubbing with nylon film 30 times prior to each experiment. The open-circuit voltage, short-circuit current, and short-circuit charge of the SNC-TENG were measured using a Keithley 6514 electrometer. During demonstration of the potential applications of the SNC-TENG, an Arduino Uno was employed as the signal acquisition unit, while a NVIDIA Jetson Nano was used to activate the surveillance camera.

Supporting Information

Supporting Information is available from the Wiley Online Library or from the author.

Conflict of Interest

The authors declare no conflict of interest.

Data Availability Statement

The data that support the findings of this study are available from the corresponding author upon reasonable request.

[1] J. Wei, J. M. Snider, J. Kim, J. M. Dolan, R. Rajkumar, B. Litkouhi, in *2013 IEEE Intelligent Vehicles Symp.*, IEEE, Piscataway, NJ **2013**, pp. 763–770.

[2] T.-D. Vu, O. Aycard, F. Tango, in *2014 IEEE Intelligent Vehicles Symp. Proc.*, IEEE, Piscataway, NJ **2014**, pp. 774–780.

[3] H. Zhu, K. V. Yuen, L. Mihaylova, H. Leung, *IEEE T. Intell. Transp.* **2017**, *18*, 2584.

[4] J. Van Brummelen, M. O'Brien, D. Gruyer, H. Najjaran, *Transport. Res. C-Emer.* **2018**, *89*, 384.

[5] D. Gruyer, V. Magnier, K. Hamdi, L. Claussmann, O. Orfila, A. Rakotonirainy, *Annu. Rev. Control* **2017**, *44*, 323.

[6] E. J. C. Nacpil, Z. Wang, M. Guan, K. Nakano, I. Jeon, *IEEE Sens. J.* **2023**, *23*, 16013.

[7] J. H. Shin, J. Kwon, J. U. Kim, H. Ryu, J. Ok, S. Joon Kwon, H. Park, T. il Kim, *npj Flexible Electron.* **2022**, *6*, 32.

[8] S. Campbell, N. O'Mahony, L. Krpalcova, D. Riordan, J. Walsh, A. Murphy, C. Ryan, in *2018 29th Irish Signals and Systems Conf.*, IEEE, Piscataway, NJ **2018**, pp. 1–4.

[9] T. S. Combs, L. S. Sandt, M. P. Clamann, N. C. McDonald, *Am. J. Prev. Med.* **2019**, *56*, 1.

[10] J. M. Armingol, J. Alfonso, N. Aliane, M. Clavijo, S. Campos-Cordobés, A. de la Escalera, J. del Ser, J. Fernández, F. García, F. Jiménez, in *Intelligent Vehicles*, Elsevier, Amsterdam **2018**, pp. 23–101.

[11] H. Lee, M. Ra, W. Y. Kim, *IEEE Access* **2020**, *8*, 48049.

[12] X. Tang, H. Song, W. Wang, Y. Yang, *Sensors* **2020**, *20*, 6517.

[13] R. Heinzler, P. Schindler, J. Seekircher, W. Ritter, W. Stork, *IEEE Intelligent Vehicles Symp. Proc.*, IEEE, Piscataway, NJ **2019**, p. 1527.

[14] A. N. Catapang, M. Ramos, in *2016 6th IEEE Int. Conf. Control System, Computing and Engineering*, IEEE, Piscataway, NJ **2016**, pp. 441–445.

[15] G.-R. Liu, M.-Z. Zhou, L.-L. Wang, H. Wang, in *2016 Int. Conf. on Information System and Artificial Intelligence*, IEEE, Piscataway, NJ **2016**, pp. 479–484.

[16] S. X. Li, Y. X. Cao, X. Bi, in *Advances in Materials Research*, Trans Tech Publications, Stafa-Zurich, Switzerland **2013**, pp. 1008–1012.

[17] D. L. McCollum, C. Wilson, M. Bevione, S. Carrara, O. Y. Edelenbosch, J. Emmerling, C. Guivarch, P. Karkatsoulis, I. Keppo, V. Krey, Z. Lin, E. Broin, L. Paroussos, H. Pettifor, K. Ramea, K. Riahi, F. Sano, B. S. Rodriguez, D. P. van Vuuren, *Nat. Energy* **2018**, *3*, 664.

**ADVANCED
SCIENCE NEWS**

www.advancedsciencenews.com

**ADVANCED
FUNCTIONAL
MATERIALS**

www.afm-journal.de

[18] Y. Tang, W. Xuan, C. Zhang, L. Xu, F. Liu, J. Chen, H. Jin, Z. Ye, Z. Cao, Y. Li, J. Luo, *Nano Energy* **2021**, *89*, 106429.

[19] J. Yang, Y. Sun, J. Zhang, B. Chen, Z. L. Wang, *Cell Rep.* **2021**, *2*, 100666.

[20] S. Li, Z. Zhao, D. Liu, J. An, Y. Gao, L. Zhou, Y. Li, S. Cui, J. Wang, Z. L. Wang, *Adv. Mater.* **2022**, *34*, 2110363.

[21] J. Liu, P. Xu, J. Zheng, X. Liu, X. Wang, S. Wang, T. Guan, G. Xie, M. Xu, *Nano Energy* **2022**, *101*, 107633.

[22] Y. Wang, D. Liu, Z. Hu, T. Chen, Z. Zhang, H. Wang, T. Du, S. L. Zhang, Z. Zhao, T. Zhou, M. Xu, *Adv. Mater. Technol.* **2021**, *6*, 2001270.

[23] Y. Wang, Z. Hu, J. Wang, X. Liu, Q. Shi, Y. Wang, L. Qiao, Y. Li, H. Yang, J. Liu, L. Zhou, Z. Yang, C. Lee, M. Xu, *ACS Appl. Mater. Interfaces* **2022**, *14*, 24832.

[24] M. Xu, S. Wang, S. L. Zhang, W. Ding, P. T. Kien, C. Wang, Z. Li, X. Pan, Z. L. Wang, *Nano Energy* **2019**, *57*, 574.

[25] C. Zhao, D. Liu, Y. Wang, Z. Hu, Q. Zhang, Z. Zhang, H. Wang, T. Du, Y. Zou, H. Yuan, X. Pan, J. Mi, M. Xu, *Nano Energy* **2022**, *94*, 106926.

[26] Y. C. Lai, J. Deng, S. L. Zhang, S. Niu, H. Guo, Z. L. Wang, *Adv. Funct. Mater.* **2017**, *27*, 1604462.

[27] Y. C. Lai, J. Deng, R. Liu, Y. C. Hsiao, S. L. Zhang, W. Peng, H. M. Wu, X. Wang, Z. L. Wang, *Adv. Mater.* **2018**, *30*, 1801114.

[28] Y. C. Lai, H. W. Lu, H. M. Wu, D. Zhang, J. Yang, J. Ma, M. Shamsi, V. Vallem, M. D. Dickey, *Adv. Energy Mater.* **2021**, *11*, 2100411.

[29] Z. H. Guo, H. L. Wang, J. Shao, Y. Shao, L. Jia, L. Li, X. Pu, Z. L. Wang, *Sci. Adv.* **2022**, *8*, 5201.

[30] S. M. S. Rana, M. A. Zahed, M. T. Rahman, M. Salauddin, S. H. Lee, C. Park, P. Maharjan, T. Bhatta, K. Shrestha, J. Y. Park, *Adv. Funct. Mater.* **2021**, *31*, 2105110.

[31] J. W. Lee, S. Jung, J. Jo, G. H. Han, D. M. Lee, J. Oh, H. J. Hwang, D. Choi, S. W. Kim, J. H. Lee, C. Yang, J. M. Baik, *Energy Environ. Sci.* **2021**, *14*, 1004.

[32] Y. Tang, H. Zhou, X. Sun, N. Diao, J. Wang, B. Zhang, C. Qin, E. Liang, Y. Mao, *Adv. Funct. Mater.* **2020**, *30*, 1907893.

[33] S. A. Han, W. Seung, J. H. Kim, S. W. Kim, *ACS Energy Lett.* **2021**, *6*, 1189.

[34] D. V. Anaya, K. Zhan, L. Tao, C. Lee, M. R. Yuce, T. Alan, *Nano Energy* **2021**, *90*, 106486.

[35] J. Ma, J. Zhu, P. Ma, Y. Jie, Z. L. Wang, X. Cao, *ACS Energy Lett.* **2020**, *5*, 3005.

[36] H. Guo, X. Jia, L. Liu, X. Cao, N. Wang, Z. L. Wang, *ACS Nano* **2018**, *12*, 3461.

[37] S. Peng, Y. Feng, Y. Liu, M. Feng, Z. Wu, J. Cheng, Z. Zhang, Y. Liu, R. Shen, D. Wang, *Nano Energy* **2022**, *104*, 107899.

[38] Y. Xi, J. Hua, Y. Shi, *Nano Energy* **2020**, *69*, 104390.

[39] F. Wang, Z. Ren, J. Nie, J. Tian, Y. Ding, X. Chen, *Adv. Mater. Technol.* **2020**, *5*, 1900789.

[40] F. Yuan, S. Liu, J. Zhou, S. Wang, Y. Wang, S. Xuan, X. Gong, *Nano Energy* **2021**, *86*, 106071.

[41] W. Zhang, Y. Lu, T. Liu, J. Zhao, Y. Liu, Q. Fu, J. Mo, C. Cai, S. Nie, *Small* **2022**, *18*, 2200577.

[42] X. Luo, L. Zhu, Y. C. Wang, J. Li, J. Nie, Z. L. Wang, *Adv. Funct. Mater.* **2021**, *31*, 2104928.

[43] S. Wang, Y. Xie, S. Niu, L. Lin, C. Liu, Y. S. Zhou, Z. L. Wang, *Adv. Mater.* **2014**, *26*, 6720.

[44] M. Salauddin, S. M. S. Rana, M. Sharifuzzaman, M. T. Rahman, C. Park, H. Cho, P. Maharjan, T. Bhatta, J. Y. Park, *Adv. Energy Mater.* **2021**, *11*, 2002832.

[45] K. Dong, Z. Wu, J. Deng, A. C. Wang, H. Zou, C. Chen, D. Hu, B. Gu, B. Sun, Z. L. Wang, *Adv. Mater.* **2018**, *30*, 1804944.

[46] Y. C. Lai, J. Deng, S. Niu, W. Peng, C. Wu, R. Liu, Z. Wen, Z. L. Wang, *Adv. Mater.* **2016**, *28*, 10024.

[47] Y. Tian, Y. An, B. Xu, *Nano Energy* **2022**, *101*, 107556.

[48] W. T. Cao, H. Ouyang, W. Xin, S. Chao, C. Ma, Z. Li, F. Chen, M. G. Ma, *Adv. Funct. Mater.* **2020**, *30*, 2004181.

[49] Z. L. Wang, *Faraday Discuss.* **2014**, *176*, 447.

[50] K. Shi, B. Chai, H. Zou, D. Min, S. Li, P. Jiang, X. Huang, *Research* **2022**, *2022*, 9862980.

[51] D. W. Kim, J. H. Lee, I. You, J. K. Kim, U. Jeong, *Nano Energy* **2018**, *50*, 192.

[52] F. Jiang, X. Zhou, J. Lv, J. Chen, J. Chen, H. Kongcharoen, Y. Zhang, P. S. Lee, *Adv. Mater.* **2022**, *34*, 2200042.

[53] H. Riazi, G. Taghizadeh, M. Soroush, *ACS Omega* **2021**, *6*, 11103.

[54] Y. Zheng, Y. Wang, Z. Li, Z. Yuan, S. Guo, Z. Lou, W. Han, G. Shen, L. Wang, *Matter* **2023**, *6*, 506.

[55] Y. Ma, Y. Yue, H. Zhang, F. Cheng, W. Zhao, J. Rao, S. Luo, J. Wang, X. Jiang, Z. Liu, N. Liu, Y. Gao, *ACS Nano* **2018**, *12*, 3209.

[56] Z. Yuan, Q. Lin, Y. Li, W. Han, L. Wang, *Adv. Mater.* **2023**, *35*, 2211527.

[57] L. Sun, Z. Wang, C. Li, W. Tang, Z. Wang, *Nano energy Adv.* **2023**, *3*, 1.

[58] C. X. Lu, C. B. Han, G. Q. Gu, J. Chen, Z. W. Yang, T. Jiang, C. He, Z. L. Wang, *Adv. Eng. Mater.* **2017**, *19*, 1700275.

[59] E. Thakran, S. Bhattacharya, S. Verma, *Int. J. Tech. Res. Sci.* **2020**, *Special*, 108.

[60] R. Zallone, in *2020 AEIT Int. Conf. of Electrical and Electronics Technologies for Automotive (AEIT AUTOMOTIVE)*, IEEE, Piscataway, NJ **2020**, pp. 1–6.

[61] B. Park, J. H. Shin, J. Ok, S. Park, W. Jung, C. Jeong, S. Choy, Y. J. Jo, T. Il Kim, *Science* **2022**, *376*, 624.

[62] G. Liu, M. Zhou, L. Wang, H. Wang, X. Guo, *Optik* **2017**, *135*, 353.

2306381 (12 of 12)